Energy Advances

ROYAL SOCIETY OF CHEMISTRY

PAPER

View Article Online
View Journal | View Issue

Check for updates

Cite this: *Energy Adv.*, 2022, 1, 690

Thermal decomposition of ammonium nitrate (AN) in the presence of the optimized nano-ternary transition metal ferrite $CoNiZnFe_2O_4$†

Pragnesh N. Dave * and Ruksana Sirach

Received 16th June 2022,
Accepted 22nd August 2022

DOI: 10.1039/d2ya00146b

rsc.li/energy-advances

$CoNiZnFe_2O_4$ was synthesized and characterized using techniques such as powder XRD, Raman spectroscopy, and infrared (IR) spectroscopy. The optical band-gap energy and thermal stability of $CoNiZnFe_2O_4$ were also explored. The effect of 2% by mass of $CoNiZnFe_2O_4$ on the thermal decomposition of ammonium nitrate (AN) was studied using simultaneous thermal analysis (TG-DTA). The presence of $CoNiZnFe_2O_4$ in AN converts the endothermic curve of AN into an exothermic curve with a reduction in the peak temperature by 20 °C. The kinetic investigations suggest that the thermal decomposition of AN + $CoNiZnFe_2O_4$ occurs at a lower activation energy (by 76 kJ mol^{-1}) with a decreased pre-exponential factor (by 0.4 min^{-1}), suggesting a faster decomposition of AN in the presence of $CoNiZnFe_2O_4$. The findings of the present work suggest that AN + $CoNiZnFe_2O_4$ can be used in place of pure AN as an oxidizer in military applications.

Solid-propellant oxidizers are widely used in the preparation of high-energy fuels, which are broadly used in propellants, explosives, and pyrotechnic formulations for rockets, missiles and space vehicles having military, and civil applications. To achieve fast efficiency of propellant oxidizers additives are added to improve its decomposition process, which is easily prepared, easily separable, and environmentally friendly.[1–4] Research in the field of thermolysis of propellant oxidizers, namely ammonium perchlorate (AP), 3-nitro-2,4-dihydro-3*H*-1,2,4-triazol-5-one (NTO), ammonium nitrate (AN), 1,3,5,7-tetranitro-1,3,5,7-tetrazocane (HMX), 1,3,5-trinitroperhydro-1,3,5-triazine (RDX), and hexanitrohexaazaisowurtzitane (CL-20), is capturing increasing interest from decades to the present day for the enhancement of their decomposition performance, thermal stability, detonation properties, thermal sensitivity, and toxicity.[3,5–9] Among these oxidants, AN is the widely used oxidizing agent due to its low-temperature and chlorine-free decomposition, which can replace AP-based propulsion systems.[1,10–12] AN-Based energetic materials are high in oxygen content, and upon decomposition, a large amount of heat and gaseous products are released.[13–15] The additives such as metals, metal oxides, organic–inorganic oxides, ferrites, and bimetal oxides have been reported to enhance the thermal decomposition of AN.[16–18] Moreover, the ability of metal oxides/ferrites to serve as a bridge in the electron or proton transfer process from the decomposed products of the AN molecule is a preliminary step of decomposition while complete decomposition occurs with the evolution of gaseous products. Nowadays, nano-transition metals with spinel structures having ferrimagnetic properties and high catalytic activity are used as an additive for AN-type propulsion systems to reduce their thermal decomposition temperature, attracting considerable interest in rocket propellant systems.[19–21] The decomposition of AN in the presence of additives can be completely endothermic, exothermic, or endo–exothermic, while pure AN decomposes with only the endothermic phase.[22,23] The theoretical and experimental decomposition peak temperatures of pure AN were at around 300 °C.[24] Among the various preparation methods, sol–gel, aging, hydrothermal, and co-precipitation methods are widely used to prepare nano-sized materials.[10] A lot of work on quaternary ferrites as an additive on AP has been performed, which suggested a good effect of ferrites of later transition metal ions such as Co, Cu, Ni, and Zn on the thermal decomposition of AP. However, the effect of quaternary ferrite has not been studied to the best of our knowledge. Hence, in the present work, we explored the effect of nano-$CoNiZnFe_2O_4$ on the thermal decomposition of ammonium nitrate that can be used as a replacement for AN in rocket applications. Further, the kinetic parameters of AN in the presence of $CoNiZnFe_2O_4$ were investigated to study the activation energy and pre-exponential factor of AN, both of which are important parameters for determining the ease and speed of the decomposition process. Isoconversional approaches are among the most dependable kinetic methods for dealing with thermoanalytical data. Kinetic investigations using thermoanalytical data were extensively used to investigate the speed and energy of the high energetic materials to evaluate their decomposition performance.[25,26]

Department of Chemistry, Sardar Patel University, Vallabh Vidyanagar, 388 120, Gujarat, India. E-mail: Pragnesh7@yahoo.com

† Electronic supplementary information (ESI) available. See DOI: https://doi.org/10.1039/d2ya00146b

In this communication, nano-additive tri-transition metal ferrite $CoNiZnFe_2O_4$ was prepared using a co-precipitation method in which a strong base act as a precipitating agent. Various instrumental techniques, such as XRD, Raman FE-SEM, FTIR, and UV-visible spectroscopy methods were used to investigate the optical, structural, and morphological properties of nano-$CoNiZnFe_2O_4$. In this work, to calculate the catalytic performance of spinel ferrite $CoNiZnFe_2O_4$ for the thermolysis of AN, the kinetic parameters such as activation energy and pre-exponential factor of AN decomposition with and without $CoNiZnFe_2O_4$ were obtained from the thermal analysis techniques using the Arrhenius relation.

Nano-additive $CoNiZnFe_2O_4$ preparation method

Hydrated forms of ferric nitrate, cobalt nitrate, nickel nitrate, zinc nitrate, and sodium hydroxide were purchased from Loba Chemie India. All the reagents were of analytical grade and used as received without further purification. The solutions were prepared using triple distilled water. Iron nitrate and other metal nitrates were taken in the 2 : 1 molar ratio and dissolved in 100 ml purified water. 2 M NaOH solution was prepared and added dropwise into nitrate solutions with continuous stirring until complete precipitation of their hydroxides was achieved, at this point, the pH of the solution was 12. Further, the powder was collected by vacuum filtration and also purified by washing it with warm water. The powder was dried at 70 °C in an oven, and calcined at 350 °C for 4 h in a muffle furnace to form spinel ferrite from their hydroxide complex. These $CoNiZnFe_2O_4$ particles were physicochemically characterized using a preliminary XRD tool and secondary tools FE-SEM, UV-Vis, Raman spectroscopy, FTIR spectroscopy, and TG-DTA.

Structural analysis

The powder X-ray diffraction (XRD) of the co-precipitated freshly prepared tri-transition metal spinel ferrite $CoNiZnFe_2O_4$ was obtained on an Ultima-IV X-ray diffractometer at 40 mA and 40 kV in the 2θ range of 10°–90° using CuKα radiation having a wavelength of 1.5406 Å. Further, the obtained pattern was evaluated using the Powder-X software, and crystalline size was calculated using the Scherrer's equation[27] using Highscore+ software (PDF No: 96-591-0065; Fig. S2, ESI†). Fig. 1(a) shows the XRD pattern of the calcined sample of $CoNiZnFe_2O_4$ ferrite. The main diffraction peaks were: 2θ values 18.6°, 30.7°, 35.8°, 36.3°, 43.4°, 57.4°, and 62.9°, and corresponding diffraction planes (111), (220), (311), (222), (400), (511), and (440), respectively. The absence of the additional peaks revealed that the sample had a single-phase cubic spinel structure with cell parameters $a = b = c$ (Å) and $\alpha = \beta = \gamma = 90$ (°). Peak belonging to the 311 plane (35.8°) was used to calculate the crystalline size using the Scherrer's equation. The obtained crystalline size was in the range of 9–28 nm, confirming the formation of a single-phase nanocrystalline $CoZnNiFe_2O_4$.

The Raman spectrum of $CoNiZnFe_2O_4$ nano-spinel ferrite is shown in Fig. 1(b) while the spectra of pure AN and its mixture with $CoNiZnFe_2O_4$ are shown in Fig. 2. The room temperature Raman scattering spectra were measured on a micro-Raman spectrometer STR 500, JobinYvon Horiba LabRam, HR800, with a diode laser (532 nm, 25 mW) as an excitation source. This spectrometer is equipped with a charge-coupled device detector giving a spectral resolution of ~1 cm^{-1} in the 50 cm^{-1} to 1700 cm^{-1} wavenumber ranges. A total of five Raman active modes were found to be present in $CoNiZnFe_2O_4$ between 100–1200 cm^{-1}, which was in agreement with the previous studies.[28,29] The peaks found between 100 cm^{-1} and 800 cm^{-1} correspond to $3T_{2g}$, E_g, and A_{1g} molecular orbitals belonging to the polarized stretching and bending modes of metal–metal and metal–oxygen bonds (Zn–O; Ni–O; Co–O; Fe–O). Moreover, peaks present at Raman shift 800 cm^{-1} to 1200 cm^{-1} are associated with ternary metals and spinel-structured metal oxides molecular vibrations. The peaks were obtained at higher Raman shifts compared to those from previous studies.[28,29] This could be assigned to the size effect of the nanoparticles.

The vibrational characteristics of the molecules were investigated by Raman and IR spectroscopy techniques. Here, Fourier transform infrared spectrum (FTIR) spectrum of a ferrite sample was analyzed on the FTIR-8400S, Shimadzu spectrophotometer. The FTIR spectrum of spinel ferrite $CoNiZnFe_2O_4$ is displayed in Fig. 1(c). The spectrum is in the fingerprint region of 4000–500 cm^{-1} wavenumbers. The characteristic peaks of tri-transition metal ferrite include broad metal–oxygen bands between 1000 cm^{-1} and 500 cm^{-1}, stretching vibration of O–H between 3800 cm^{-1} and 3000 cm^{-1}, C–O stretching vibration between 3000 cm^{-1} and 2000 cm^{-1}, bending vibration of N–O and H–O–H bonds between 2000 cm^{-1} and 1000 cm^{-1}, and significantly important peaks observed at 590 cm^{-1} and are assigned to iron–oxygen (Fe–O) bonds with respect to other metal–oxygen (M–O such as Zn–O, Co–O, and Ni–O); stretching vibration confirmed the presence of spinel ferrite structured nanomaterials.[30] Some of the vibrational modes are obtained due to the hygroscopic nature of the ferrite that absorbs atmospheric gaseous molecules.

UV-Visible spectroscopy of $CoNiZnFe_2O_4$ ferrite nanoparticles was performed on a Shimadzu UV-1800 spectrophotometer and the plot of absorbance *vs.* wavelength is displayed in Fig. 1(d). The peak for the absorbance of the $CoNiZnFe_2O_4$ nanoparticles was found between 200 nm and 400 nm, corresponding to the absorbance peak at 300 nm. The lower wavelength absorbance indicates the formation of nanoparticles. Additionally, the indirectly allowed transition energy band gap was evaluated by extrapolating the line of plot between $(\alpha h\nu)^2$ *vs.* energy $(h\nu)$ using Tauc's relation.[31] The estimated E_g value of the ferrite sample was 2.75 eV and it was associated with the allowed direct transition between the conduction band and valence band. The lower band gap energy of the $CoNiZnFe_2O_4$ could help the electronic movement in the AN + $CoNiZnFe_2O_4$ composite during the decomposition of AN, facilitating the decomposition process. UV-Vis can be used to determine the optical property of the material and it provides information on the size-dependent

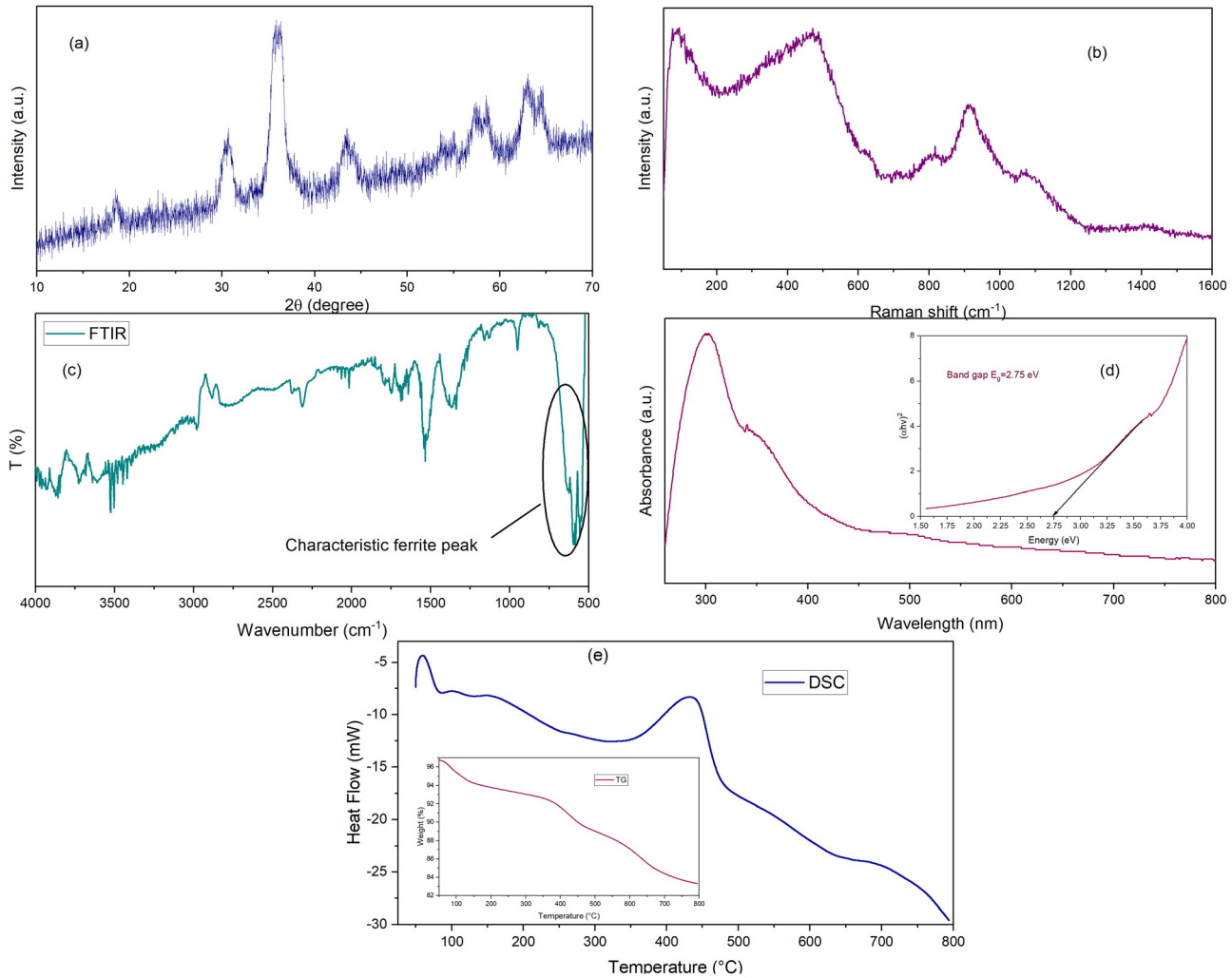

Fig. 1 Characterization results of $CoNiZnFe_2O_4$ material (a) powder XRD, (b) Raman, (c) FTIR, (d) UV-visible, (e) TG-DSC.

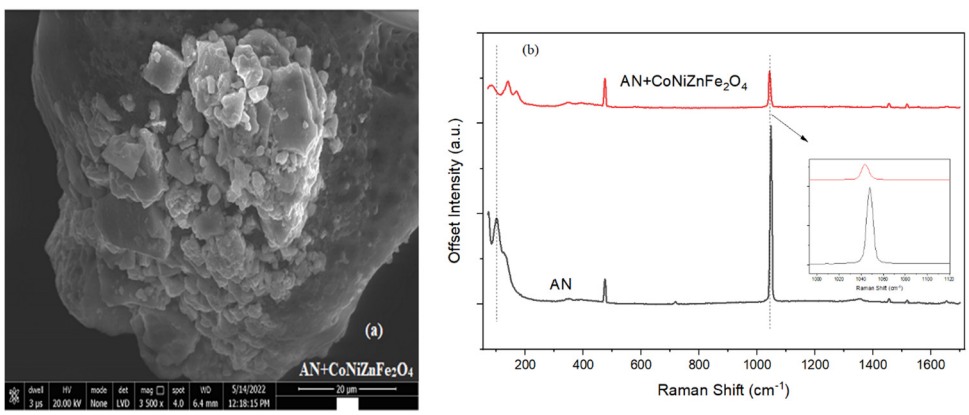

Fig. 2 (a) FE-SEM image of AN + $CoNiZnFe_2O_4$ (b) Raman scattering of pure AN and AN + $CoNiZnFe_2O_4$.

spectrum, indicating a decrease in the size of the particle shifts the absorbance peak towards a lower wavelength, *i.e.*, blue shift.

TG-DSC analysis was performed on a simultaneous thermal tool equipped with a DSC-60 detector under a nitrogen atmosphere at 50 °C to 800 °C temperatures using a platinum pan. The thermal decomposition pattern of the calcined ferrite sample is displayed in Fig. 1(e). It gives details about the influence of temperature on the thermal stability of $CoNiZnFe_2O_4$

material. TG-DSC curve shows a three-stage mass loss or endothermic decomposition; the first stage is the lower temperature mass loss assigned to the evaporation of water molecule; the second stage is a moderate broad temperature range mass loss assigned to the formation of hydroxide complex, and the third stage is high-temperature loss assigned to ternary metal spinel ferrite structural lattice rearrangements.[32]

The morphology of AN with the additive nano-ferrite $CoNiZnFe_2O_4$ was captured on the Nova nano FEG-SEM 450 using a high-resolution low-vacuum field emission gun. Its image is shown in Fig. 2(a), and the upper phase morphology is associated with the polyhedron shape of $CoNiZnFe_2O_4$ nanoparticles and has agglomeration, while the lower phase is the AN morphology, which has large hallow granules with a rough surface. Moreover, the SEM results are analogous to the XRD data. However, the particle sizes differ from crystalline sizes due to the agglomeration of polycrystalline particles.

Fig. 2(b) shows the Raman scattering spectra for the detection of the explosive precursor, ammonium nitrate (AN), and a mixture of AN + $CoNiZnFe_2O_4$. The spectra show both sharp and broad bands. Pure AN has peaks in the Raman shift region of 50 cm^{-1} to 1700 cm^{-1}, in which <200 cm^{-1} Raman bands are attributed to the stretching and bending vibrations of the pyramid symmetry; Raman bands between 300 cm^{-1} and 800 cm^{-1} correspond to the symmetric and asymmetric stretching vibrations of the nitrate ions NO_3^- and tetrahedral units of NH_4^+, respectively; Raman bands between 900 cm^{-1} and 1200 cm^{-1} correspond to the symmetric stretching vibrations of O–N–O type dimer or terminating group linkages of the NO_3^- bond; and the Raman bands between 1300–1700 cm^{-1} correspond to the vibrational modes of the ammonium ion deformation or hygroscopic nature of AN.[33]

Moreover, in the presence of $CoNiZnFe_2O_4$, the peaks corresponding to the stretching and bending modes of $NH_4^+NO_3^-$ shifted from a lower frequency to a higher frequency. This implies that the Raman bands are affected by frequency shifts in the presence of $CoNiZnFe_2O_4$, while the higher frequency bands disappear. However, the intensity and area of all the peaks was decreased in the presence of $CoNiZnFe_2O_4$. It can be seen that in the presence of $CoNiZnFe_2O_4$, the Raman peaks become shorter and shift towards the right-hand side, indicating a blue shift occurring due to the size effect of the nanoparticles except for the peak $\sim$1040 cm^{-1}. This peak exhibits a red shift. The reason could have been the weakening of the bond between the ammonium ion and the nitrate ion.[20] The change in Raman spectra in this additive is related to a change in the strength of the bond due to tri-metal spinel ferrite-induced lattice-volume expansion and anharmonic interaction between the phonon modes.[20,34] The Raman analysis further confirmed the formation of $CoNiZnFe_2O_4$ nano-phase particles.

Herein, the efficient effect of tri-transition metal ferrite $CoNiZnFe_2O_4$ on the thermolysis of AN is introduced. Hence, TG-DTG-DTA analyses were performed on a simultaneous thermal analyzer STA7200, Hitachi, in an inert N_2 atmosphere from room temperature to 400 °C temperature at 5, 10, and 15 °C min^{-1} heating rates. The thermo-analytical curves of AN thermal decomposition with nano ferrite $CoNiZnFe_2O_4$ are presented in Fig. 4 (TG-DTG) and Fig. 5 (DTA).

The decomposition of pure AN (Fig. 3) shows five endothermic phases in the temperature range of 50 °C to 350 °C: phase I has an orthorhombic system from 50 °C to 75 °C, phase II has a tetragonal system at 75 °C to 120 °C, phase III has cubic symmetry at 125 °C to 150 °C, phase IV has a melting temperature at around 170 °C, and phase V has a decomposition peak temperature at around 300 °C. As for most energetic materials, the thermolysis of AN depends on various factors such as pressure, temperature, and experimental conditions, such as sample mass, heating rates, sample purity, monitoring techniques, and the presence of foreign substances, which may further influence the thermal stability of an AN-based material. The complete reaction mechanism is still under further research, which could then explain all aspects of the decomposition properties. Here, some known reaction steps that are given as follows:[35–37]

$$NH_4NO_3 \rightarrow NH_{3(g)} + HNO_{3(g)} \quad (1)$$

$$2HNO_3 = NO_2^+ + NO_3^- + H_2O \quad (2)$$

$$NH_4NO_3 \rightarrow N_2O + 2H_2O \quad (3)$$

$$NH_4NO_3 \rightarrow 2N_2 + O_2 + 4H_2O \quad (4)$$

$$HNO_3 \rightarrow NO_2 + OH^{\bullet} \quad (5)$$

The thermal decomposition mechanism of AN includes two ways: one involves a proton or electron transfer endothermic reaction, where melted AN is decomposed into gaseous products, which occurs at low temperatures with relatively low speed (eqn (1) and (2)). The second way is a radical reaction that occurs at a high temperature and can be exothermic (eqn (3)–(5)). In the presence of additive spinel ferrite, AN decomposition is improved as the additive provides active sites for the proton or electron transfer reactions that decreased the decomposition peak temperature for AN compared to that of pure AN, which further impacted kinetic parameters. After catalytic endothermic decomposition of AN, the exothermic peak observed due to its high-temperature heating may lead to HNO_3 decomposition to the free-radical formation, which happens in some circumstances only.

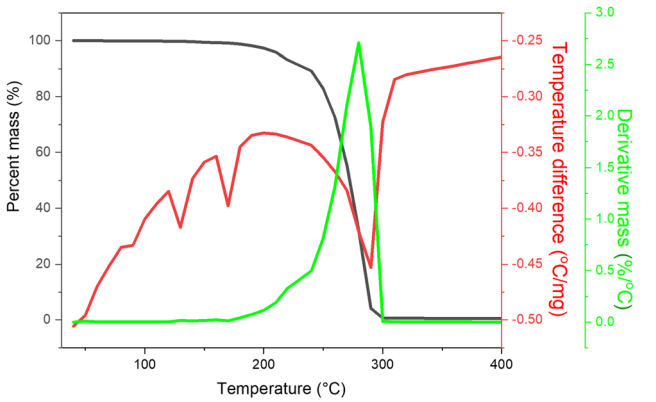

Fig. 3 TG, DTG, and DTA (EXO UP) curve of pure AN.

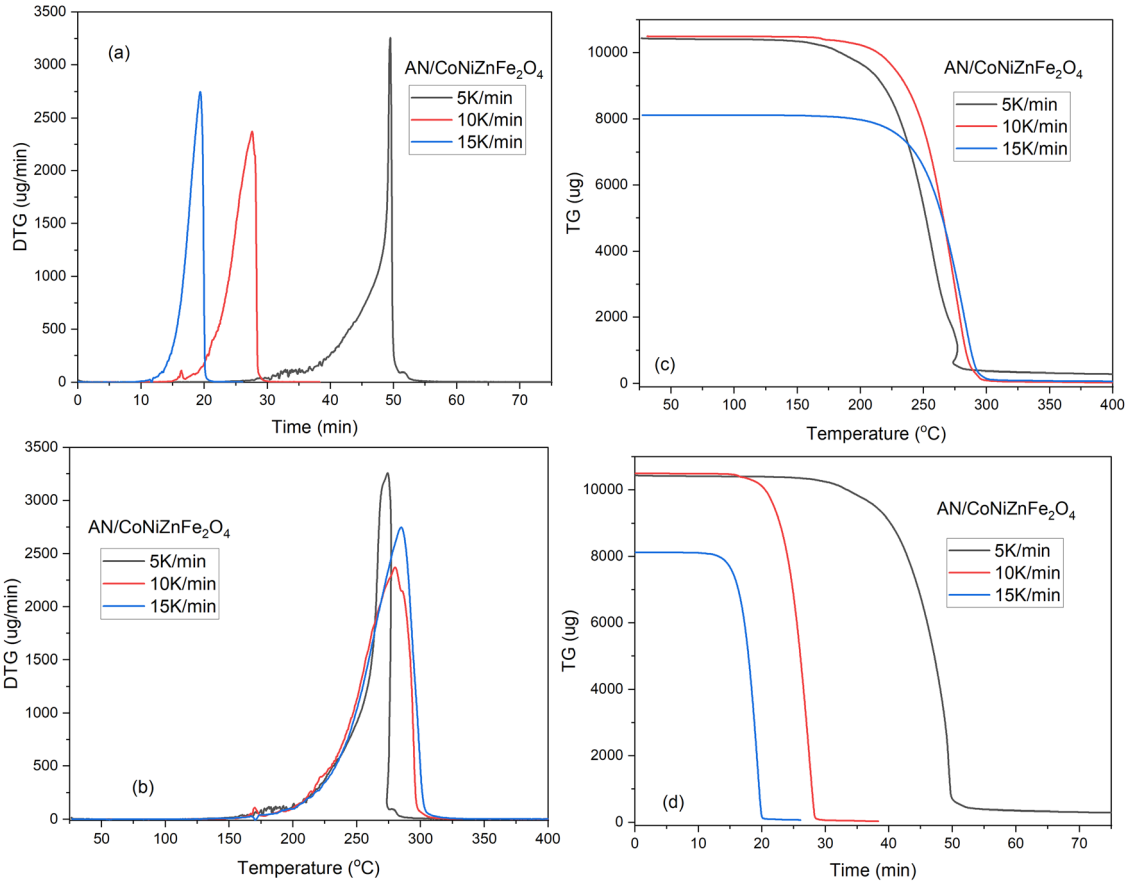

Fig. 4 TG-DTG analyses of AN/$CoNiZnFe_2O_4$ with 5, 10, and 15 °C min^{-1} heating rates.

The TG-DTG curves of AN + $CoNiZnFe_2O_4$ revealed the mass change over time and temperature at three different heating rates (Fig. 4). The slower the sample is heated, the longer it takes for the reaction to complete (Fig. 4(a)). The temperature effect was reversed, indicating that when heating rates were increased, the peak temperature increased as well (Fig. 4(b)). Heating rates of 5 °C min^{-1} and 10 °C min^{-1} resulted in two stages of decomposition, whereas heating rates of 15 °C min^{-1} resulted in a single stage of breakdown. However, TG curves were also associated with DTG in terms of time study; at a greater heating rate, the sample required less time, while the temperature study revealed that the mass loss of the sample occurred at a higher heating rate.

The heating rate, type of additive, and atmospheric condition strongly affect the thermolysis and stability of AN. With increasing heating rates, the exothermic and endothermic peaks shift to the right. In the presence of additive nano-$CoNiZnFe_2O_4$, the temperature at which decomposition begins is lower than that for pure ammonium nitrate, and eventually, it went more rapidly from the endothermic phase to the Sharp exothermic phase. That indicates increased thermal stability and it was observed at a 5 °C min^{-1} heating rate (Fig. 5). The tetragonal phase also disappeared for 5 μV mg^{-1} DTA analysis. However, for the 10 °C min^{-1} heating rate, the tetragonal phase appears and the endothermic decomposition of AN occurred, while for the 15 °C min^{-1} heating rate

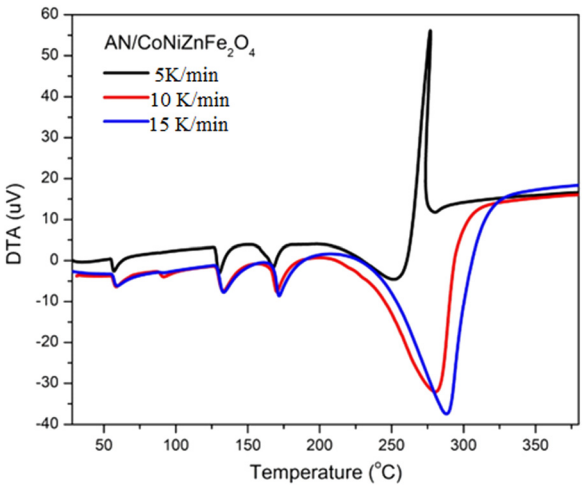

Fig. 5 DTA analysis of AN/$CoNiZnFe_2O_4$ at 5, 10, and 15 °C min^{-1} heating rates.

the tetragonal phase disappeared, and the endo-phase decomposition peak shifted to the right side. The AN + $CoNiZnFe_2O_4$ mixture decomposes similarly to AN except that the endotherm of AN (~290 °C) is converted to exotherm (~270 °C) in the presence of $CoNiZnFe_2O_4$, which has also been reported in previous literature.[2,38–40] The exotherm for AN + $CoNiZnFe_2O_4$ is

Table 1 Thermolysis and kinetic data of AN and AN with nano-$CoNiZnFe_2O_4$

Sample/parameters	Pure AN	AN + $CoNiZnFe_2O_4$
Phase transition (°C)	56.3	55.5
	88.2	88.4 (at 10 °C min^{-1}) (Fig. 5)
	132.4	126.8
Melting (°C)	169.5	166.7
Decomposition (°C)	290.4	254.9 (endothermic peak)
		270.4 (exothermic at 5 °C min^{-1}) (Fig. 5)
E_a (kJ mol^{-1})	158 ± 1	82 ± 1
$\ln A$ (min^{-1})	4.2 ± 3	3.8 ± 1

most likely due to the additional breakdown of the intermediates at this temperature, where the exothermic decomposition begins about 270.4 °C at 5 K min^{-1} or °C min^{-1} heating rates.

Kinetic stability

When a catalyst is applied in a chemical reaction, it can either speed up or slow down the reaction. The catalyst speeds up the reaction by suppressing the reaction's activation energy by creating an alternative route that requires less energy and it is more favorable. DTA data can be used to estimate the activation energy using a kinetic relation.[35–37,41] The decomposition peak temperature of AN in the presence of the $CoNiZnFe_2O_4$ nano-catalyst is reduced by 10 °C to 40 °C with varying heating rates. Accordingly, the activation energy of AN is also decreased by ~47%, indicating its great catalytic activity for reducing the thermal decomposition of AN. With the increase in the heating rate, the decomposition peak temperature also increased.

$$\ln\left(\frac{\beta}{T_p^2}\right) = \ln\left(\frac{AR}{E_k}\right) - \frac{E_k}{RT_p} \quad (1)$$

where β is the heating rate, T_p is the decomposition peak temperature, A is the Arrhenius constant calculated from the intercept of the plot, E_k is the activation energy or kinetic energy evaluated from the slope, and R is the universal gas constant. The thermal decomposition and kinetic findings are listed in Table 1.

Comparison with other studies

In one of the previous studies, Vara *et al.*[2,40] investigated the effect of 1% by mass on bimetallic transition metal oxides and ferrites on the thermal decomposition of ammonium nitrate and their use as a burning rate catalyst. In their study, they found that as the decomposition temperature of AN decreased, the burning rate of corresponding propellants also increased. Although the authors observed a decrement in the peak temperature of AN, in the case of all the additives, (Table 2) best results were obtained for AN + CuZnO (279 °C). In the present work, we have advanced further by decreasing the peak temperature of AN up to 270 °C for the AN + $CuNiZnFe_2O_4$ system. However, the exothermic peak temperature of AN + $CuNiZnFe_2O_4$ was quite higher than that of the co-crystal of hydrazine 3-nitro-1,2,4-triazol-5-one (HNTO) and AN (227 °C), which was further reduced up to 149 °C by incorporating the energetic graphene oxide–triaminoguanidine–cobalt complex (GO–T–Co–T). The same was also verified by the formation of propellants by similar authors.[38,39,42] However, it is to be noted that the co-crystal systems contain other high energetic materials other than AN, and therefore, the thermal property of the co-crystal is the mutual effect of both the energetic materials, while in our work it is because the variation in the thermal behaviour of AN alone as $CoNiZnFe_2O_4$ itself is not a high energetic material. Hence, AN + $CoNiZnFe_2O_4$ can be used as a highly energetic oxidizer in hydroxyl-terminated polybutadiene (HTPB)-based propellants in place of AN for better thermal performance.

In conclusion, we provided various characterization methodologies for the tri-transition metal ferrite $CoNiZnFe_2O_4$ propellant oxidizer additive. Although thermolysis experiments on AN + $CoNiZnFe_2O_4$ have revealed an efficient, lower crystalline size, active vibrational modes, easy separability, and reusable magnetic properties including nano-ferrite material, we believe that this represents a wide spectrum of nano-sized particles. Importantly, this allows the prediction of the active ferro–ferri catalytic sites, which has promising implications for high-efficiency catalysis and other propulsion applications. The effect of the heating rate on AN with $CoNiZnFe_2O_4$ thermolysis under constant atmospheric conditions demonstrated its potential performance in this system. The additive shows a promising effect by lowering the decomposition temperature of AN by 20 °C despite low additive content (2% by mass) along with a decrement in the activation energy and pre-exponential factor compared to pure AN. As a result, this system's outstanding catalytic performance makes it easy to prepare mixed metal spinel-type oxides for composite propellants and can be used in a range of explosive devices.

Table 2 Comparison of the decomposition peak temperature of AN in the presence of various additives

Catalyst	Additive content (%)	Exo peak temperature of AN containing catalyst (°C)	Ref.
NiZnO	1	287	2
CoZnO	1	285	2
$CuNiFe_2O_4$	1	282	40
CuZnO	1	279	2
$CoNiZnFe_2O_4$	2	270	Present work
HNTO/AN co-crystal	[a]	227	38
HNTO–AN/GO–T–Co–T	[a]	149	39

[a] Not applicable.

Author contributions

Pragnesh N. Dave and Ruksana Sirach contributed to data curation, formal analysis, methodology, investigation, validation, and writing of the original draft of this manuscript. Pragnesh N. Dave contributed to the conceptualization, funding acquisition, project administration, resources, supervision, visualization, and writing – review, and editing of this manuscript.

Conflicts of interest

The authors declare no known conflicts of interest.

Acknowledgements

We acknowledge the Department of Chemistry and Department of Physics, Sardar Patel University for providing a research facility, the use of the various instrumental tools, and helpful support services till the completion of work. We are grateful to the Sophisticated Instrumentation Centre for Applied Research and Testing (SICART), Charutar Vidya Mandal University, Vallabh Vidyanagar, Anand, Gujarat, for availing FE-SEM instrument facility. We are thankful to the project funding agency, Department of Science and Technology, India (SR/NM/NT-1014/2016(G)) for the junior research fellowship, research associate fellowship, and other research expenses.

Notes and references

1 Z. Cheng, X. Chu, J. Yin, B. Dai, W. Zhao, Y. Jiang, J. Xu, H. Zhong, P. Zhao and L. Zhang, *Chem. Eng. J.*, 2020, **385**, 123859.
2 J. A. Vara and P. N. Dave, *Chem. Phys. Lett.*, 2019, **730**, 600–607.
3 M. Yang, X. Chen, Y. Wang, B. Yuan, Y. Niu, Y. Zhang, R. Liao and Z. Zhang, *J. Hazard. Mater.*, 2017, **337**, 10–19.
4 B. J. Wood and H. Wise, *J. Chem. Phys.*, 1955, **23**, 693–696.
5 J. H. MacNeil, H.-T. Zhang, P. Berseth and W. C. Trogler, *J. Am. Chem. Soc.*, 1997, **119**, 9738–9744.
6 A. Cabrera, C. R. Torres, L. Juncal, M. Meyer and S. Stewart, *Appl. Energy Combust. Sci.*, 2021, **6**, 100026.
7 H. B. Wu, M. N. Chan and C. K. Chan, *Aerosol Sci. Technol.*, 2007, **41**, 581–588.
8 Y. Wang, X. Song and F. Li, *ACS Omega*, 2019, **4**, 214–225.
9 V. Babrauskas and D. Leggett, *Fire Mater.*, 2020, **44**, 250–268.
10 I. Oluwoye, M. Altarawneh, J. Gore and B. Z. Dlugogorski, *Combust. Flame*, 2020, **213**, 132–139.
11 M. Kohga and S. Togo, *Combust. Flame*, 2018, **192**, 10–24.
12 Z. Han, S. Sachdeva, M. I. Papadaki and M. S. Mannan, *J. Loss Prev. Process Ind.*, 2015, **35**, 307–315.
13 C. Oommen and S. Jain, *J. Hazard. Mater.*, 1999, **67**, 253–281.
14 J. C. Oxley, J. L. Smith, E. Rogers and M. Yu, *Thermochim. Acta*, 2002, **384**, 23–45.
15 Z. Xu, G. Xu, X. Fu and Q. Wang, *Cent. Eur. J. Energ. Mater.*, 2017, **14**, 636–659.
16 N. M. Hadi, M. R. Mohammad and H. G. Abdulzahraa, *Al-Nahrain Journal of Science*, 2017, **20**, 60–66.
17 R. M. Kannaujiya, S. H. Chaki, A. J. Khimani, Z. R. Parekh and M. Deshpande, *Chem. Thermodyn. Therm. Anal.*, 2022, **6**, 100058.
18 R. Gunawan and D. Zhang, *J. Hazard. Mater.*, 2009, **165**, 751–758.
19 S. Chaturvedi and P. N. Dave, *J. Energy Mater.*, 2013, **31**, 1–26.
20 D. Diaz and D. W. Hahn, *Spectrochim. Acta, Part A*, 2020, **233**, 118204.
21 S. Ganesan and B. Sridhar, *Int. J. Mech. Mechatron.*, 2014, **4**, 110–115.
22 Y. Izato, K. Shiota and A. Miyake, *J. Anal. Appl. Pyrolysis*, 2019, **143**, 104671.
23 M. Kaniewski, K. Hoffmann and J. Hoffmann, *Thermochim. Acta*, 2019, **678**, 178313.
24 X. Wang, C. Pei, X. Wu, F. Xu, N. Yang, D. Liu and S. Xu, *J. Loss Prev. Process Ind.*, 2022, **77**, 104780.
25 D. Trache, A. Abdelaziz and B. Siouani, *J. Therm. Anal. Calorim.*, 2017, **128**, 335–348.
26 A. F. Tarchoun, D. Trache, T. M. Klapötke, K. Slimani, B. Belouettar, A. Abdelaziz, S. Bekhouche and W. Bessa, *Propellants, Explos., Pyrotech.*, 2022, **47**, e202100293.
27 S. A. El-Sayed, *J. Anal. Appl. Pyrolysis*, 2022, **161**, 105364.
28 C. Cherpin, D. Lister, F. Dacquait and L. Liu, *Materials*, 2021, **14**, 2557.
29 A. Miri, M. Sarani, A. Najafidoust, M. Mehrabani, F. A. Zadeh and R. S. Varma, *Mater. Res. Bull.*, 2022, **149**, 111706.
30 D. Mukherjee, N. Sen, K. Singh, S. Saha, K. Shenoy and P. Marathe, *Sens. Actuators, A*, 2021, **331**, 112927.
31 Y. Izato and A. Miyake, *J. Therm. Anal. Calorim.*, 2015, **122**, 595–600.
32 S. N. Rishikeshi and S. Joshi, *J. Therm. Anal. Calorim.*, 2012, **109**, 1473–1479.
33 H.-Q. Cao, Q.-L. Duan, H. Chai, X.-X. Li and J.-H. Sun, *J. Hazard. Mater.*, 2020, **384**, 121297.
34 J. I. Contreras-Rascón, J. Díaz-Reyes, S. Luna-Suárez, R. C. Carrillo-Torres and R. Sánchez-Zeferino, *Thin Solid Films*, 2019, **692**, 137609.
35 Z.-X. Xu, J.-H. Cheng, Q. Wang, J. Cheng and X. Hu, *J. Therm. Anal. Calorim.*, 2019, **136**, 1415–1424.
36 Y. Izato and A. Miyake, *J. Therm. Anal. Calorim.*, 2018, **134**, 813–823.
37 S. A. Skarlis, A. Nicolle, D. Berthout, C. Dujardin and P. Granger, *Thermochim. Acta*, 2014, **584**, 58–66.
38 S. Hanafi, D. Trache, R. Meziani, H. Boukciat, A. Mezroua, A. F. Tarchoun and M. Derradji, *Chem. Eng. J.*, 2021, **417**, 128010.
39 S. Hanafi, D. Trache, A. Mezroua, H. Boukeciat, R. Meziani, A. Fouzi Tarchoun and A. Abdelaziz, *RSC Adv.*, 2021, **11**, 35287–35299.
40 J. A. Vara, P. N. Dave and S. Chaturvedi, *Part. Sci. Technol.*, 2021, **39**, 1–9.
41 Q. Wu, L. Tan, S. Xu, D. Liu and L. Min, *J. Energy Mater.*, 2018, **36**, 202–210.
42 S. Hanafi, D. Trache, R. Meziani, H. Boukeciat, A. F. Tarchoun, A. Abdelaziz and A. Mezroua, *FirePhysChem*, 2022, DOI: 10.1016/j.fpc.2022.07.003.